Specific cation effects at aqueous solution-vapor interfaces: surfactant-like behavior of Li^+ revealed by experiments and simulations

Kathryn A. Perrine[a,1], Krista M. Parry[a,1], Abraham C. Stern[a], Marijke H. C. Van Spyk[a], Michael J. Makowski[a], Bernd Winter[b], Douglas J. Tobias[a,2], John C. Hemminger[a,2]

[a]Department of Chemistry, University of California Irvine, Irvine, California, USA 92697-2025, United States

[b]Department of Molecular Physics, Fritz-Haber-Institut der Max-Planck-Gesellschaft, Faradayweg 4-6, 14195 Berlin, Germany

[1]These authors contributed equally to this work.

[2]To whom correspondence should be addressed. E-mail: dtobias@uci.edu or jchemmin@uci.edu

Author contributions: B.W., D.J.T., and J.C.H. conceived the study; K.A.P., M.H.C.V.S., M.J.M, B.W., and J.C.H. performed the experiments; K.M.P and A.C.S. carried out the molecular dynamics simulations; K.A.P., K.M.P., A.C.S., M.H.C.V.S., M.J.M., and B.W. analyzed the data; K.A.P., K.M.P., D.J.T., and J.C.H. wrote the manuscript.

Keywords: specific ion effects, Hofmeister series, aqueous interfaces, photoelectron spectroscopy, molecular dynamics simulations

Abstract

It is now well established by numerous experimental and computational studies that the adsorption propensities of inorganic anions conform to the Hofmeister series. The adsorption propensities of inorganic cations, such as the alkali metal cations, have received relatively little attention. Here we use a combination of liquid-jet X-ray photoelectron experiments and molecular dynamics simulations to investigate the behavior of K^+ and Li^+ ions near the interfaces of their aqueous solutions with halide ions. Both the experiments and the simulations show that Li^+ adsorbs to the aqueous solutionvapor interface, while K^+ does not. Thus, we provide the first experimental validation of the "surfactant-like" behavior of Li^+ predicted by previous simulation studies. Furthermore, we use our simulations to trace the difference in the adsorption of K^+ and Li^+ ions to a difference in the resilience of their hydration shells.

Significance

Ion adsorption to the interfaces of aqueous salt solutions plays a key role in a wide variety of chemical and biochemical processes. For example, the adsorption of ions to the surface of aqueous aerosol particles in the atmosphere influences their reactivity to gas-phase oxidants. While the so-called chaotropic anions (e.g., I^-, SCN^-, and ClO_4^-) are known to have strong adsorption propensities, inorganic cations are generally regarded as being repelled from aqueous solution-air interfaces. Here we report a concerted experimental and computational study that reveals that Li^+ adsorbs to the interfaces of aqueous lithium halide solutions and, hence, is an exceptional cation.

\body

Myriad chemical and biochemical processes that occur in aqueous salt solutions exhibit trends that depend systematically on the identities of the salt ions. These trends, which are commonly referred to as specific ion effects, generally follow the Hofmeister series, a ranking of the ability of salt ions to precipitate proteins that was developed by Franz Hofmeister and co-workers in the late 1800s (1). The Hofmeister series applies, however, to a wide range of other seemingly unrelated phenomena, such as colloidal stability, critical micelle concentrations, chromatographic selectivity, protein denaturation temperatures, and the interfacial properties of aqueous salt solutions (2, 3). Early attempts to explain the Hofmeister series relied on the notion that salt ions have a long-range effect on the structure of water, with ions on one side of the series acting as "structure makers" and ions on the other side as "structure breakers" (2, 4). However, more recently, several experimental and computational studies have questioned the role of long-range ordering/disordering effects (4-9), and have provided compelling evidence that ion-specific behavior at aqueous interfaces must be taken into consideration when attempting to explain Hofmeister effects (7, 10-13).

Specific anion effects on the interfacial properties of aqueous salt solutions, such as surface tensions and surface potentials, closely follow the Hofmeister series for anions (14). For example, surface tension increments (differences between the surface tension of a salt solution and that of neat water) of sodium salts at the same concentration decrease in the order: $SO_4^{2-} > Cl^- > Br^- > NO_3^- > I^-$ (15, 16). Molecular dynamics (MD) simulations have predicted that the propensity of anions to adsorb to the solution–vapor interface follows the Hofmeister series in reverse (7, 14, 17), and this prediction has largely been confirmed experimentally (14, 18-22). Moreover, MD simulations have shown that, with few exceptions, anions adsorb more strongly

to the solution-air interface than their counter-cations and, consequently, electrical double layers are formed near the interface, with the anions residing in or near the topmost layer of the solution, and the cations below the anions (14, 23, 24). Surface potentials (25), phase-sensitive vibrational sum frequency generation (PS-VSFG) spectra (22, 26, 27), and x-ray photoelectron spectroscopic (XPS) data (19, 28-31) are consistent with the double layer picture.

Compared to anion-specific effects, cation-specific effects at the solution-air interface are generally observed to be relatively weak. For example, the concentration dependence of the surface tension increments of LiCl, NaCl, and KCl are very similar (32). In one of the few studies that directly determined cation-specific effects on ion distributions in the interfacial region, XPS spectra and MD simulations revealed that Na^+ approaches the solution-air interface more closely than Rb^+, and that the interfacial population of Cl^- is greater in NaCl vs. RbCl solutions (30). PS-VSFG measurements, which provide indirect information on interfacial ion distributions via surface electric fields inferred from the imaginary part of the nonlinear susceptibility, have provided evidence of cation-specific effects on the strength of the electric double layer at the solution-air interfaces of nitrate, sulfate, and halide salt solutions (22, 26, 27).

In almost all aqueous solutions of inorganic salts, cations are excluded from the topmost layer of the solution (14). It has been suggested, based on MD simulations (33-35), that Li^+ may be an exception. Presently, Li^+ is the only metal cation that has been observed in MD simulations to exhibit the "surfactant-like" behavior displayed by certain anions. However, this theoretical prediction has not been confirmed experimentally. Here we report liquid-jet XPS (LJ-XPS) measurements of the interfacial ion distributions in potassium and lithium halide solutions that provide direct experimental evidence that, indeed, Li^+ adsorbs to the solution-air interface, while K^+ does not. We also report MD simulations that qualitatively reproduce the LJ-XPS results and

provide molecular-level insights into the origin of the differences in the behavior of Li^+ and K^+ at the solution-air interface.

Results and Discussion

Depth-dependent cation/water-oxygen ratios from LJ-XPS spectra. LJ-XPS signals originating from the I4d and K2p orbitals in 2 M KI, and I4d and Li1s orbitals in 2 M LiI, are shown in Fig. 1*A-C* for both low (probing the surface) and high (probing the bulk) photoelectron kinetic energies (KE). Comparison of the low (200 eV) and high (600 eV) KE spectra reveals that the I^- signal is greater at low KE than at high KE for both the KI (Fig. 1*A*) and LiI (Fig. 1*C*) solutions, consistent with the now well-established notion that the population of I^- ions is greater at the surface vs. the bulk in alkali iodide solutions (14, 19, 24). The K^+ signal is lower at low KE than at high KE (Fig. 1*B*), indicating a depletion of K^+ ions at the surface relative to the bulk of the KI solution, which is also consonant with the prevailing picture of ion distributions near the surfaces of aqueous alkali halide solutions (14, 24). In contrast, the Li^+ signal at low KE is significantly higher than that at high KE (Fig. 1*C*). Thus, the spectra in Fig. 1*C* provide the first direct experimental confirmation of the prediction, made on the basis of MD simulations (33-35), that Li^+ ions adsorb to the aqueous solution-air interface.

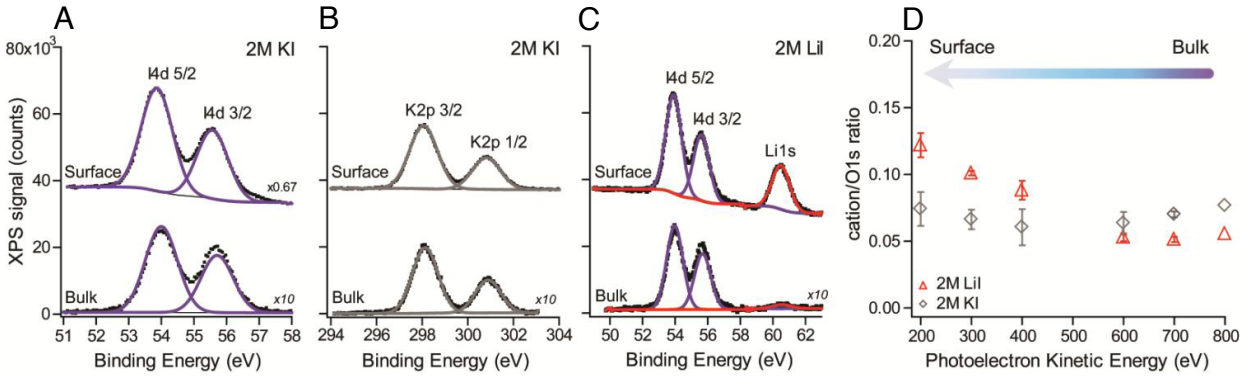

Fig. 1. (*A*) Surface (200 eV KE) and bulk (600 eV KE) LJ-XPS spectra for (*A,B*) 2 M KI solutions and (*C*) LiI solutions. (*D*) Ratios of normalized cation/O1s signals plotted vs. photoelectron KE (probe depth).

The integrated area under each spectral curve in Figs. 1*A*-*C* provides a measure of the concentration of each ion at a particular probe depth of the experiment. To this end, the peak areas are first normalized by their respective photoionization cross section, photon flux, detection angle, and the electron transmission of the analyzer, as described in detail in the Materials and Methods section (28, 36, 37). To obtain ion concentrations, the normalized ion spectral peak areas are divided by the normalized water O1s peak area at the same photoelectron KE. Fig. 1*D* compares the ratio of normalized cation/O1s signals from 2 M KI and LiI solutions as a function of photoelectron KE (eV) or experimental probe depth. The cation to oxygen ratios in the bulk (photoelectron KE $\geq$ 600 eV) of both the KI and LiI solutions exhibit the expected bulk stoichiometry within experimental statistics, thus validating our approach for obtaining depth profile information using LJ-XPS. While the K2p/O1s ratio remains essentially constant at all depths probed, the Li1s/O1s ratio exceeds the bulk stoichiometric ratio in the interfacial region (photoelectron KE $\leq$ 400 eV) and increases as the probing depth (photoelectron KE) decreases. Thus, the data in Fig. 1*C* clearly show that the concentration of Li^+ ions near the surface of a 2 M LiI solution is greater than in the bulk, i.e., that Li^+ is displaying surfactant-like behavior.

The cation to water oxygen ratios shown in Fig. 1*C* as a function of photoelectron KE for 2 M KI and LiI solutions are compared to the corresponding results for other 2 M K^+ and Li^+ halide salt solutions (KCl, KBr, LiCl, and LiBr) in Fig. S2*A*-*B*. In all cases, the K2p/O1s ratios are essentially constant at all depths probed (200 eV to 800 eV) (Fig. S2*A*). As in the case of LiI (Fig. 1C), the Li1s/O1s ratios also increase with decreasing probe depth in LiCl and LiBr (Fig. S2*B*). At the lowest photoelectron KEs considered, the Li1s/O1s ratio increases in the order LiCl < LiBr < LiI. Thus, the extent of Li^+ adsorption tracks the reverse Hofmeister ordering of anion adsorption ($Cl^- < Br^- < I^-$) observed in previous XPS experiments(19) and MD simulations,(23)

as well as the new anion/O1s ratios measured as a function of photoelectron KE reported in Fig. S2*C-D*.

Depth-dependent anion/cation ratios from LJ-XPS spectra. Anion/cation ratios were determined from the XPS spectra by following the same procedure used to obtain the cation/O1s ratios. The I4d/K2p and I4d/Li1s ratios in the 2 M KI and 2 M LiI solutions, respectively, are plotted vs. photoelectron KE (probing depth) in Fig. 2. The I^-/K^+ ratio is greater than unity at the lowest photoelectron KE (200 eV) measured, indicating an excess of I^- anions over K^+ cations near the surface of the KI solution. This result is qualitatively consistent with previous XPS measurements (19), but the surface I^-/K^+ ratio in the present study is lower, presumably, in part, because the previous measurements were carried out on a deliquesced solid (saturated solution), whereas the measurements reported herein were carried out on a 2 M solution. The I^-/Li^+ ratio in 2 M LiI remains essentially constant near unity over the entire range of photoelectron KE (Fig. 2). This result is consistent with our observation that both the Li^+/water O (Fig. 1*A*) and I^-/water O (Fig. S2*D*) ratios are greater, to roughly the same extent, at the solution surface than in the bulk. Thus, the anion/cation ratios confirm that Li^+ exhibits surfactant-like behavior, similar to I^-, while K^+ does not.

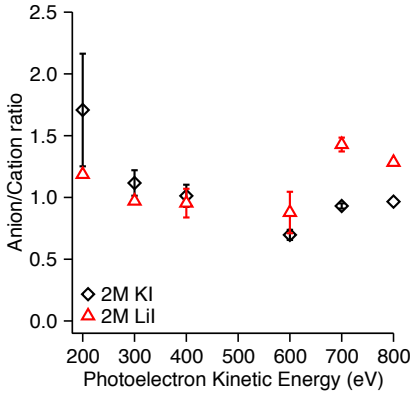

Fig. 2. Ratios of normalized XPS signals (I4d/K2p for KI and I4d/Li1s for LiI) plotted vs. photoelectron KE (probe depth) for 2 M KI and 2 M LiI solutions.

The LJ-XPS data reported in Figs. 1 and 2 were measured at a 20˚ angle between the polarization vector and the detection axis To confirm that our findings are not affected by electron emission anisotropy, in a separate experiment we measured the depth profile of 2 M LiI in comparison to 2 M NaI solutions at the magic angle (54.7˚), where electron emission anisotropy is eliminated. In this case, only the orbital photoionization cross sections are needed to obtain the ion concentration ratios (28, 37). The data measured at the magic angle for 2 M NaI and LiI solutions (Fig. S1) confirm that the ion concentration ratios are independent of the experimental geometry. Given that the results are independent of the scattering angle, we collected the most complete set of data at a 20° scattering angle where the signals are stronger.

Anion/cation ratios for 2 M KCl, KBr, and KI solutions are compared in Fig. S3*A* and those for 2 M LiCl, LiBr, and LiI solutions are compared in Fig. S3*B*. The anion/K^+ ratio at the lowest photoelectron KE measured decreases in the order KI > KBr ~ KCl (Fig S3*A*). The anion/Li^+ ratios at the lowest photoelectron KE are slightly less than one for the LiCl and LiBr solutions (Fig. S3*B*), indicating that Li^+ ions are present with the anions in the interfacial region of those solutions.

Density profiles from MD simulations. Density profiles for ions and water oxygen atoms, computed from MD simulations of 2 M KI and 2 M LiI solutions and divided by the corresponding bulk densities (ρ_0), are plotted in Fig. 3 vs. the distance from the instantaneous solution-air interface (i.e., depth into the solution). Referring the density profiles to the instantaneous interface (see *SI Appendix* for definition and method of calculation) reveals structure in the interfacial region that is obscured when mean density profiles are computed on a static grid (38, 39). The water density profiles in Fig. 3 each display two peaks, one at ~2 Å and the other at ~5 Å below the interface, and the iodide density profiles display sharp peaks on the

inner side of the topmost water layer, followed by a depletion zone centered around 5 Å below the interface, in which the ion density is lower than in the bulk. To maintain the electroneutrality of the interfacial region, the density profiles of the cations also contain peaks corresponding to enhanced ion populations in the interfacial region vs. the bulk. Both the K^+ (in KI) and Li^+ (in LiI) density profiles indicate enhanced populations in the zone of I^- depletion below interfacial peak in the I^- density profiles. In addition, the Li^+ density profile displays a more prominent peak that is coincident with I^- interfacial peak. Thus, the MD simulation of 2 M LiI recapitulates the "surfactant-like" behavior of Li^+ inferred from the LJ-XPS data (Figs. 1 and 2).

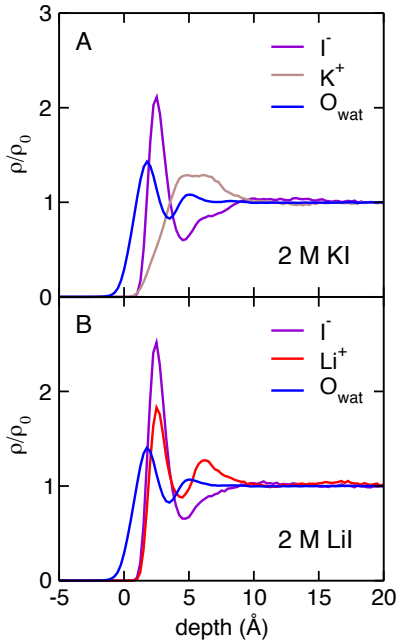

Fig. 3. Density profiles of ions and water oxygen atoms from MD simulations of (*A*) 2 M KI and (*B*) 2 M LiI solutions. The density profile of each species has been calculated with respect to the instantaneous solution-air interface and divided by the corresponding bulk density, ρ_0. The interface is located at depth = 0.

The anion density profiles for K^+ and Li^+ solutions of all three halides considered show signal corresponding to surface-adsorbed anions that decreases in the order $I^- > Br^- > Cl^-$ (Figure S4). As for K^+ in the KI solution, the K^+ density profiles from the KBr and KCl solutions do not

contain peaks corresponding to surface-adsorbed K^+ ions (Figure S4*A*-*C*). On the other hand, as in the case of Li^+ in LiI, the Li^+ density profiles from the LiBr and LiCl solutions display a peak (for LiBr) or shoulder (for LiCl) corresponding to surface-adsorbed anions (Figure S4*D*-*F*). Thus, the "surfactant-like" behavior of Li^+ adsorption observed in the LiI solution is also seen in the LiBr and LiCl solutions, albeit to a lesser extent, and decreasing in the order LiI > LiBr > LiCl.

Origins of the different interfacial propensities of Li^+ and K^+ ions. We can use our MD simulations to address the question of why Li^+ adsorbs to the topmost layer of water but K^+ does not. Although the relative importance of the various forces that drive ions toward or away from aqueous solution-air interfaces is a subject of on-going inquiry (39-44), there is broad consensus that cavity formation promotes ion adsorption, and the loss of dispersion and local (hydration shell) electrostatic interactions accompanying ion desolvation opposes ion adsorption. In addition, when point-charge models are used for the ions and water molecules, as in the present study, there is an electrochemical surface potential, arising from broken symmetry in the water structure at ion-water and air-water interfaces, that favors the adsorption of anions and opposes the adsorption of cations (40, 41). In finite concentration solutions, such as those considered here, it is also possible that ion-ion interactions are different in bulk solution than in the interfacial region; in this case, there will be an additional electrostatic contribution to an ion's adsorption propensity.

The cavity term clearly does not contribute to the greater adsorption propensity of Li^+ vs. K^+ because K^+ is larger than Li^+. As we shall see below, Li^+ retains its full solvation shell even when it is in the topmost water layer, while K^+ sheds part of its solvation shell as it approaches the surface of the solution. Due to the loss of water molecules in the K^+ solvation shell, the

concomitant loss of dispersion interactions opposes K^+ adsorption. On the other hand, since Li^+ retains its full solvation shell at the interface, the difference in dispersion interactions between Li^+ at the interface and in the bulk should be negligible. Thus, dispersion interactions are not expected to play an appreciable role in the adsorption of Li^+.

Next we examine the ion-ion and ion-water electrostatic interactions. The total electrostatic potential energy of K^+ ions in 2 M KI and Li^+ ions in 2 M LiI, as well as the contributions of cation-cation, cation-anion, and cation-water interactions, are plotted as functions of depth into the solutions in Fig. 4*A*-*B*. Not surprisingly, the cation-cation electrostatic interaction energies are repulsive throughout each solution, and the shapes of the energy profiles resemble the shapes of the cation density profiles (Fig. 4*C*-*D*). The cation-anion electrostatic interaction energies are attractive throughout each solution, and the cation-anion interaction energy profiles are essentially mirror images of the cation-cation profiles. Thus, since these cation interactions balance throughout the solution, the cation-ion electrostatic interactions do not contribute considerably to the adsorption propensity of either K^+ in 2 M KI or Li^+ in 2 M LiI.

The cation-water electrostatic interactions are attractive throughout each solution, and relatively very weak compared to the cation-cation and cation-anion electrostatic interactions (Fig. 4*A*-*B*). For K^+ in the KI solution, there is a very shallow minimum in the cation-water electrostatic interaction energy profile (Fig. 4*A*), spanning roughly the same range of depth (~4–9 Å) as that of the enhanced K^+ density corresponding to the subsurface layer of K^+ ions (Fig. 4*C*). Upon moving closer to the interface the K^+–water electrostatic energy rises to zero as the number of water molecules in the K^+ hydration shell drops from its bulk value of six (Fig. 4*E*). Thus, desolvation constitutes a small penalty to the adsorption of K^+ ions to the solution surface. Likewise, the Li^+–water electrostatic interaction energy profile displays minima (Fig. 4*B*) where

the Li^+ density profile contains maxima (Fig. 4*D*), with the deepest minimum coinciding with the surface layer of Li^+ ions. The Li^+ ion is able to maintain attractive Li^+–water interactions all the way up to the solution surface because it retains its full hydration shell, consisting of four water molecules, throughout the solution (Fig. 4F; see also (33)). The same picture emerges from our MD simulations of potassium and lithium bromide (Fig. S5) and chloride (Fig. S6) solutions: in all cases attractive cation-anion electrostatic interactions are essentially canceled by repulsive cation-cation electrostatic interactions throughout each solution, K^+ loses favorable electrostatic interactions with water due to desolvation as it approaches the solution surface, and Li^+ retains its solvation shell and favorable electrostatic interactions with water molecules in the topmost layer of solution.

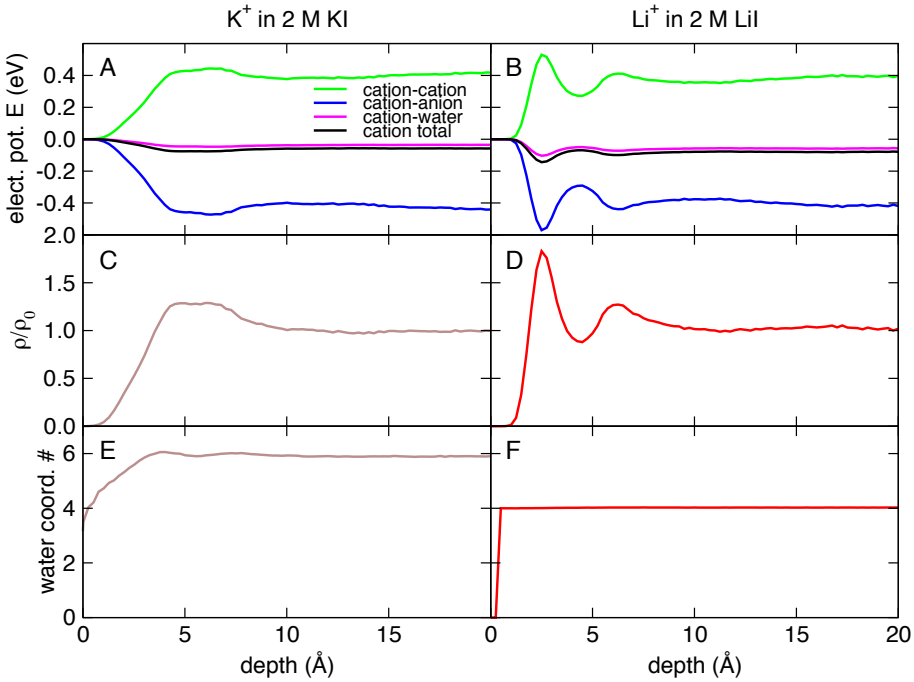

Fig. 4. Depth-dependence of the electrostatic interaction energies of (*A*) K^+ ions in 2 M KI and (*B*) Li^+ ions in 2 M LiI. The green curves are contributions from cation-cation interactions, the blue curves from cation-anion interactions, and the magenta curves from cation-water interactions. The black curves are the total electrostatic interaction energies. (*C*) Density profile for K^+ ions in 2 M KI. (*D*) Density profile for Li^+ in 2 M LiI. (*E*) Number of water molecules in the first solvation shell of K^+ in 2 M KI. (*F*) Number of water molecules in the first solvation

shell of Li^+ in 2 M LiI. All quantities in this figure were calculated with respect to the instantaneous solution-air interface. The interface is located at depth = 0.

Conclusions

We employed a combination of LJ-XPS experiments and MD simulations to investigate specific cation effects at the aqueous solution-air interfaces of potassium and lithium halide solutions. The cation/oxygen and anion/cation ratios from the LJ-XPS experiments and the density profiles from the MD simulations show that Li^+ ions adsorb to the interface, but K^+ does not. Consistent with previous studies (14, 19, 24), both the LJ-XPS experiments and MD simulations also show that the iodide anion exhibits surfactant-like behavior. Moreover, the simulations predict that the halide anion adsorption propensity decreases in the order $I^- > Br^- > Cl^-$ in both K^+ and Li^+ solutions, and that the extent of anion adsorption does not depend significantly on the identity of the counter-cation in the solutions considered here. The simulations provide evidence that the primary reason Li^+ ions are able to approach the interface more closely than K^+ is that Li^+ ions retain their full hydration shell, and the associated favorable ion-water electrostatic interactions, even in the topmost layer of the solution. In contrast, while K^+ ions retain their complete hydration shell up to the subsurface layer beneath the surface anion layer, as they approach the surface more closely they shed part of their hydration shell and lose stabilizing electrostatic interactions with water molecules.

Materials and Methods

Liquid Jet X-ray Photoelectron Spectroscopy experiments

Salt solutions were prepared by weighing out each salt and dissolving with highly demineralized water (conductivity ~0.2 μS/cm, 18.2 MΩ, deionized water), up to 100 mL. Salts were purchased, and included potassium iodide (puriss. p.a., >99.5%, Sigma Aldrich), lithium iodide (99.9% trace metals basis, Sigma Aldrich) and sodium iodide (Sigma Aldrich). All solutions

were sonicated for 5 minutes to finish dissolving the salt in the solution. The solutions were filtered, as necessary, to remove residual debris in the solutions, using sterile 0.45 um polyethersulfone membrane (VWR International) filters and sterile syringes. Each filtered solution was then degassed in the sonicator for an additional 3 minutes.

LJ-XPS is a surface sensitive technique that can determine the relative ion distributions near the surface and in the bulk of aqueous solutions. Liquid jet experiments were performed at the Molecular Environmental Sciences beamline (11.0.2) at the Advanced Light Source (ALS) at Lawrence Berkeley National Laboratory (45-49). A laminar flowing liquid microjet (Microliquids Inc.) of 21 μm diameter was generated using a 0.5 mL/min flow rate using a pulse-dampened dual piston high pressure liquid pump to allow for continuous flow of solution. An external chiller was used to hold the liquid solution at a constant temperature of 6 ˚C.

A four-stage differentially pumped lens and hemispherical analyzer system (Phoibios 150, Specs) was used for X-ray photoelectron analysis of the liquid microjet. The liquid jet was oriented normal to the axis of the near ambient pressure analyzer. The liquid jet position was placed within 0.5 mm of the analyzer aperture. The X-ray beam was oriented 70 degrees with respect to the analyzer, resulting in a 20˚ angle between the polarization of the horizontally polarized photon beam and the electron detection axis. The differential pumping and focusing of the lenses were used to allow photoelectrons to be detected by the hemispherical analyzer, kept at a base pressure of 3×10^{-9} torr with the jet in probe position with liquid water. A temperature-controlled catch basin was mounted below the liquid jet to catch the solutions. This basin was initially filled with 500 mL of a 40 wt % NaCl solution that was kept at a temperature of approximately –10 ˚C, controlled by an external ethanol chiller. The temperature controlled catch basin filled the liquid-jet chamber with 1 torr of water vapor.

Tunable linearly polarized X-ray radiation from the light source was used to probe the interface layers and the near surface region of the liquid microjet. The energy resolution of the ALS beamline varied between 150 and 853 meV for the range of photon energies used (203 to 1335 eV) for a 60 μm x 50 μm spot size. The analyzer was set to a pass energy of 20 eV with a 0.05 eV/step and a 0.1 ms dwell time. At low photoelectron kinetic energies (~200 eV), photoelectrons can escape from the interface of the flowing liquid microjet with an inelastic mean free path of approximately 10 Å.(50)

A photoelectron kinetic energy of 200 eV, used to probe the interface layers, resulted in the following photon energies for each region: 253 eV for the I4d and Li1s regions, 495 eV for the K2p region, and 735 eV for the O1s region. At high photoelectron kinetic energies (~800 eV), photoelectrons with inelastic mean free paths of up to ~30 Å can escape from deeper in the solution, characteristic of the bulk (50). A depth profile was determined by using increasing photoelectron kinetic energies including 200 eV, 300 eV, 400 eV, 600 eV, 700 eV and 800 eV. A 600 eV photoelectron KE for the bulk measurements corresponded to the following photon energies for each region: 653 eV for the I4d and Li1s regions, 895 eV for the K2p region and 1135 eV for the O1s region.

The normalization factor, as described by Yeh and Landau (36) and Ottosson et al. (28), was computed to normalize recorded XPS signals to the photon flux, transmission of the X-ray beam through 1 torr of water vapor, the atomic photoionization cross section of each respective element, and the β factor, an asymmetry factor for the electron detection that depends on orbital geometry. Although the data was not collected at the magic angle, the photoelectron anisotropy is expected to be minor for the photoelectron kinetic energies greater than 100 eV used in these experiments (37). The normalized peak areas are shown to provide an accurate measure of

relative concentrations for bulk measurements, and may also be applied to the surface data. The photon flux was recorded for each beam time using a photodiode. The X-ray transmission through water vapor was computed using the resources from the Center for X-ray optics on-line program provided by the Center for X-ray Optics at LBNL (51).

Molecular Dynamics Simulations

MD simulations of ~2 M aqueous LiCl, LiBr, LiI, KCl, KBr, and KI solutions consisted of 1728 water molecules and 68 ion pairs. The dimensions of the simulation cell were 30 Å x 30 Å x 140 Å for each system. Periodic boundary conditions were applied in all three dimensions, resulting in solution "slabs" ~70 Å thick with two solution-vacuum interfaces at $z \sim \pm 35$ Å. The SPC/E model was used for water (52), and the ion force field parameters were taken from Horinek et al. (33) (see Table S1 for a full listing of the force field parameters employed in this study). The MD trajectories were generated using the Gromacs simulation suite (53) for 80 ns each with a timestep of 1 fs; the last 70 ns of each trajectory was used for analysis. The temperature was held constant at 300 K using a Berendsen thermostat (54) with velocity rescaling to ensure the correct kinetic energy distribution (55). Water molecules were held rigid using the SETTLE algorithm (56). The electrostatic energies and forces were calculated using the particle-mesh Ewald method (57), and a cutoff of 9 Å was used to truncate the Lennard-Jones interactions and the real-space part of the Ewald sum.

Acknowledgements

This work was supported by the National Science Foundation grant CHE-0909227 and the AirUCI Organized Research Unit at the University of California, Irvine. The experiments were carried out at the Advanced Light Source (ALS) beam line 11.0.2. The ALS is supported by the Director, Office of Science, Office of Basic Energy Sciences, of the U. S. Department of Energy

under Contract No. DE-AC02-05CH11231. B.W. acknowledges support from the Deutsche Forschungsgemeinschaft (DFG) through the Collaborative Research Center 1109. We are grateful to Hendrik Bluhm and Andrey Shavorskiy for discussions and assistance with the beam line and end-station.

References

1. Hofmeister F (1888) Zur lehre von der wirkung der slaze. *Arch. Exp. Pathol. Pharmakol. (Leipzig)* 24:247-260.
2. Collins KD & Washabaugh MW (1985) The hofmeister effect and the behaviour of water at interfaces. *Q. Rev. Biophys.* 18:323-422.
3. Lo Nostro P & Ninham BW (2012) Hofmeister phenomena: An update on ion specificity in biology. *Chem. Rev.* 112:2286-2322.
4. Marcus Y (2009) Effect of ions on the structure of water: Structure making and breaking. *Chem. Rev.* 109:1346-1370.
5. Omta AW, Kropman MF, Woutersen S, & Bakker HJ (2003) Negligible effect of ions on the hydrogen-bond structure in liquid water. *Science* 301:347-349.
6. Smith JD, Saykally RJ, & Geissler PL (2007) The effects of dissolved halide anions on hydrogen bonding in liquid water. *J. Am. Chem. Soc.* 129:13847-13856.
7. Tobias DJ & Hemminger JC (2008) Chemistry - getting specific about specific ion effects. *Science* 319(5867):1197-1198.
8. Corridoni T, Mancinelli R, Ricci MA, & Bruni F (2011) Viscosity of aqueous solutions and local microscopic structure. *J. Phys. Chem. B* 115:14008-14013.
9. Funkner S*, et al.* (2012) Watching the low-frequency motions in aqueous salt solutions: The terahertz vibrational signatures of hydrated ions. *J. Am. Chem. Soc.* 134:1030-1035.
10. Vrbka L, Jungwirth P, Bauduin P, Touraud D, & Kunz W (2006) Specific ion effects at protein surfaces: A molecular dynamics study of bovine pancreatic trypsin inhibitor and horseradish peroxidase in selected salt solutions. *J. Phys. Chem. B* 110:7036-7043.
11. Zangi R, Hagen M, & Berne BJ (2007) Effect of ions on the hydrophobic interaction between two plates. *J. Am. Chem. Soc.* 129:4678-4686.
12. Pegram LM & Record Jr. MT (2008) Thermodynamic origin of hofmeister ion effects. *J. Phys. Chem. B* 112:9428-9436.
13. Zhang Y & Cremer PS (2010) Chemistry of hofmeister anions and osmolytes. *Annu. Rev. Phys. Chem.* 61:63-83.
14. Jungwirth P & Tobias DJ (2006) Specific ion effects at the air/water interface. *Chem. Rev.* 106:1259-1281.
15. Pegram LM & Record Jr. MT (2006) Partitioning of atmospherically relevant ions between bulk water and the water/vapor interface. *Proc. Natl. Acad. Sci. USA* 103:14278-14281.
16. Pegram LM & Record Jr. MT (2007) Hofmeister salt effects on surface tension arise from partitioning of anions and cations between bulk water and the air-water interface. *J. Phys. Chem. B* 111:5411-5417.

17. Dang LX & Chang T-M (2006) Recent advances in molecular simulations of ion solvation at liquid interfaces. *Chem. Rev.* 106:1305-1322.
18. Liu D, Ma G, Levering LM, & Allen HC (2004) Vibrational spectroscopy of aqueous sodium halide solutions and air-liquid interfaces: Observation of increased interfacial depth. *J. Phys. Chem. B* 108:2252-2260.
19. Ghosal S*, et al.* (2005) Electron spectroscopy of aqueous solution interfaces reveals surface enhancement of halides. *Science* 307:563-566.
20. Petersen PB & Saykally RJ (2006) On the nature of ions at the liquid water surface. *Annu. Rev. Phys. Chem.* 57:333-364.
21. Brown MA*, et al.* (2008) Ion spatial distributions at the liquid-vapor interface of aqueous potassium fluoride solutions. *Phys. Chem. Chem. Phys.* 10:4778-4784.
22. Tian C, Byrnes SJ, Han H-L, & Shen YR (2011) Surface propensities of atmospherically relevant ions in salt solutions revealed by phase-sensitive sum frequency vibrational spectroscopy. *J. Phys. Chem. Lett.* 2:1946-1949.
23. Jungwirth P & Tobias DJ (2001) Molecular structure of salt solutions: A new view of the interface with implications for heterogeneous atmospheric chemistry. *J. Phys. Chem. B* 105:10468-10472.
24. Jungwirth P & Tobias DJ (2002) Ions at the air/water interface. *J. Phys. Chem. B* 106:6361-6373.
25. Randalls JEB (1977) Structure at the free surface of water and aqueous electrolyte solutions. *Phys. Chem. Liq.* 7:107-179.
26. Hua W, Verreault D, Huang Z, Adams EM, & Allen HC (2014) Cation effects on interfacial water organization of aqueous chloride solutions. I. Monovalent cations: Li^+, na^+, k^+, nh_4^+. *J. Phys. Chem. B* 118:8433-8440.
27. Hua W, Verreault D, & Allen HC (2014) Surface electric fields of aqueous solutions of nh_4no_3, $mg(no_3)_2$, $nano_3$, and $lino_3$: Implications for atmospheric aerosol chemistry. *J. Phys. Chem. C* 118(24941-24949).
28. Ottosson N, Faubel M, Bradforth SE, Jungwirth P, & Winter B (2010) Photoelectron spectroscopy of liquid water and aqueous solution: Electron effective attenuation lengths and emission-angle anisotropy. *J. Electron Spectrosc. Relat. Phenom.* 177:60-70.
29. Ottosson N*, et al.* (2010) The influence of concentration on the molecular surface structure of simple and mixed aqueous electrolytes. *Phys. Chem. Chem. Phys.* 12:10693-10700.
30. Cheng MH*, et al.* (2012) Ambient pressure x-ray photoelectron spectroscopy and molecular dynamics simulation studies of liquid/vapor interfaces of aqueous nacl, rbcl, and rbbr solutions. *J. Phys. Chem. C* 116.
31. Tissot H*, et al.* (2015) Cation depth-distribution at alkali halide aqueous solution surfaces. *J. Phys. Chem. C* 119:9253-9259.
32. Weissenborn PK & Pugh RJ (1996) Surface tension of aqueous solutions of electrolytes: Relationship with ion hydration, oxygen solubility, and bubble coalescence. *J. Coll. Int. Sci.* 184:550-563.
33. Horinek D*, et al.* (2009) Specific ion adsorption at the air/water interface: The role of hydrophobic solvation. *Chem. Phys. Lett.* 479:173-183.
34. Bresme F, Chacon E, Tarazona P, & Wynveen A (2012) The structure of ionic aqueous solutions at interfaces: An intrinsic structure analysis. *J. Chem. Phys.* 137:114706.

35. Hahn C, Kann ZR, Faust JA, Skinner JL, & Nathanson GM (2016) Super-maxwellian helium evaporation from pure and salty water. *J. Chem. Phys.* 144:044707.
36. Yeh JJ & Lindau I (1985) Atomic subshell photoionization cross-section and asymmetry parameters - $1 < z < 103$. *At. Data Nucl. Data Tables* 32:1-155.
37. Thurmer S*, et al.* (2013) Photoelectron angular distributions from liquid water: Effects of electron scattering. *Phys. Rev. Lett.* 111:173005.
38. Willard AP & Chandler D (2010) Instantaneous liquid interfaces. *J. Phys. Chem. B* 114:1954-1958.
39. Stern AC, Baer MD, Mundy CJ, & Tobias DJ (2013) Thermodynamics of iodide adsorption at the instantaneous air-water interface. *J. Chem. Phys.* 138:114709.
40. Arslanargin A & Beck TL (2012) Free energy partitioning analysis of the driving forces that determine ion density profiles near the liquid-vapor interface. *J. Chem. Phys.* 136:104503.
41. Baer MD, Stern AC, Levin Y, Tobias DJ, & Mundy CJ (2012) Electrochemical surface potential due to classical point charge models drives anion adsorption to the air-water interface. *J. Phys. Chem. Lett.* 3:1565-1570.
42. Otten DE, Shaffer PR, Geissler PL, & Saykally RJ (2012) Elucidating the mechanism of selective ion adsorption to the liquid water surface. *Proc. Natl. Acad. Sci. USA* 109:701-705.
43. Ben-Amotz D (2016) Interfacial solvation thermodynamics. *J. Phys. Condens. Matter* 28:414013.
44. Tobias DJ, Stern AC, Baer MD, Levin Y, & Mundy CJ (2013) Simulation and theory of ions at atmospherically relevant aqueous liquid-air interfaces. *Annu. Rev. Phys. Chem.* 64:339-359.
45. Ogletree DF*, et al.* (2002) A differentially pumped electrostatic lens system for photoemission studies in the millibar range. *Rev. Sci. Instrum.* 73:3872-3877.
46. Bluhm H*, et al.* (2006) Soft x-ray microscopy and spectroscopy at the molecular environmental science beamline at the advanced light source. *Journal of Electron Spectroscopy and Related Phenomena* 150(2-3).
47. Starr DE, Wong EK, Worsnop DR, Wilson KR, & Bluhm H (2008) A combined droplet train and ambient pressure photoemission spectrometer for the investigation of liquid/vapor interfaces. *Phys. Chem. Chem. Phys.* 10:3093-3098.
48. Ogletree DF, Bluhm H, Hebenstreit ED, & Salmeron M (2009) Photoelectron spectroscopy under ambient pressure and temperature conditions. *Nucl. Instrum. Meth. A* 601:151-160.
49. Bluhm H (2010) Photoelectron spectroscopy of surfaces under humid conditions. *J. Electron Spectrosc. Relat. Phenom.* 177.
50. Olivieri G, Parry KM, Powell CJ, Tobias DJ, & Brown MA (2016) Quantitative interpretation of molecular dynamics simulations for x-ray photoelectron spectroscopy of aqueous solutions. *J. Chem. Phys.* 144:154704.
51. Henke BL, Gullikson EM, & Davis JC (1993) X-ray interactions - photoabsorption, scattering, transmission, and reflection at e=50-30,000 ev, z=1-92. *Atomic Data and Nuclear Data Tables* 54(2):181-342.
52. Berendsen HJC, Grigera JR, & Straatsma TP (1987) The missing term in effective pair potentials. *J. Phys. Chem.* 91:6269-6271.

53. Van der Spoel D*, et al.* (2005) Gromacs: Fast, flexible, and free. *J. Comput. Chem.* 26:1701-1718.
54. Berendsen HJC, Postma JPM, van Gunsteren WF, DiNola A, & Haak JR (1984) Molecular-dynamics with coupling to an external bath. *J. Chem. Phys.* 81:3684-3690.
55. Bussi G, Donadio D, & Parrinello M (2007) Canonical sampling through velocity rescaling. *J. Chem. Phys.* 126:014101.
56. Miyamoto S & Kollman PA (1992) An analytical version of the shake and rattle algorithm for rigid water models. *J. Comput. Chem.* 13:952-962.
57. Essmann U*, et al.* (1995) A smooth particle mesh ewald method. *J. Chem. Phys.* 103:8577-8593.

Supporting Information Appendix

Specific cation effects at aqueous solution-vapor interfaces: surfactant-like behavior of Li^+ revealed by experiments and simulations

Kathryn A. Perrine[a], Krista M. Parry[a], Abraham C. Stern[a], Marijke H. C. Van Spyk[a], Michael J. Makowski[a], Bernd Winter[b], Douglas J. Tobias[a], John C. Hemminger[a]

[a]Department of Chemistry, University of California Irvine, Irvine, California, USA 92697-2025, United States

[b]Department of Molecular Physics, Fritz-Haber-Institut der Max-Planck-Gesellschaft, Faradayweg 4-6, 14195 Berlin, Germany

Contents:

Materials and Methods

Definition and calculation of the instantaneous interface. All of the results from the molecular dynamics (MD) simulations are plotted vs. depth in solution. The solution surface is located using the "instantaneous interface" construction devised by Willard and Chandler (1), which involves convoluting the instantaneous density field of the water oxygen atoms and ions with Gaussian distributions:

$$\phi\left(\mathbf{r};\eta,\xi\right) = \eta\left(2\pi\xi^2\right)^{-3/2}\exp\left(-r^2/2\xi^2\right)$$

to obtain a coarse-grained density field. The location of the interface in each configuration is then taken to be the isodensity surface defined by the locus of points at which the coarse-grained density field is equal to half the bulk density of the solution. The width (ξ) and scaling (η) parameters of the Gaussians are listed in Table S1. The width parameter for the water O atoms was taken from Willard and Chandler (1). The parameters for the anions were chosen such that the local density field in a simulation of a single bulk solvated ion was homogeneous (2). The cations were not included in the convolutions because, due to their relatively small size, their contribution to the overall solution density is negligible.

Photoelectron spectra measured at the magic angle. It is possible that the geometrical anisotropy of the photoelectron emission process (3, 4) in the XPS experiments could lead to results that suggest an enhancement of the Li^+ ion concentration (relative to the I^- anion) near the surfaces of lithium halide solutions when in fact such an enhancement does not exist. To rule out this possibility, we carried out experiments in which the instrumental geometry was modified so that the polarization of the X-ray beam was at an angle of 54.7° with respect to the electron detection axis, i.e., at the so-called magic angle, where the angular anisotropy vanishes (3, 4). To determine depth profiles of the anion/cation ratios for 2 M NaI and 2 M LiI solutions, XPS spectra were measured at the magic angle for photoelectron kinetic energies ranging from 150 eV to 700 eV. At the magic angle, only the photoionization cross sections are required to obtain the anion/cation ratios. As can be seen in Figure S1, where we plot the anion/cation ratios vs. photoelectron KE obtained from XPS spectra measured at the magic angle, the observation that Li^+ ions are present near the solution surface, while Na^+ ions are depleted, persists in the absence of photoelectron emission anisotropy.

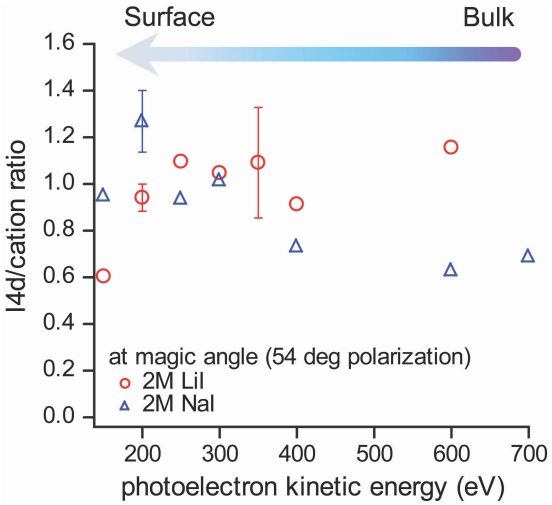

Fig. S1. Ratios of normalized XPS signals (I4d/Na2s for NaI and I4d/Li1s for LiI) plotted vs. photoelectron KE (probe depth) for 2 M NaI and 2 M LiI, obtained from XPS spectra measured with a 54.7˚ angle between the polarization of the horizontally polarized photon beam and the electron detection axis. These data are similar to the results shown in Fig. 2 of the main manuscript, indicating that our experimental observation that Li^+ ions adsorb to the solution-air interface is not an artifact of electron emission anisotropy.

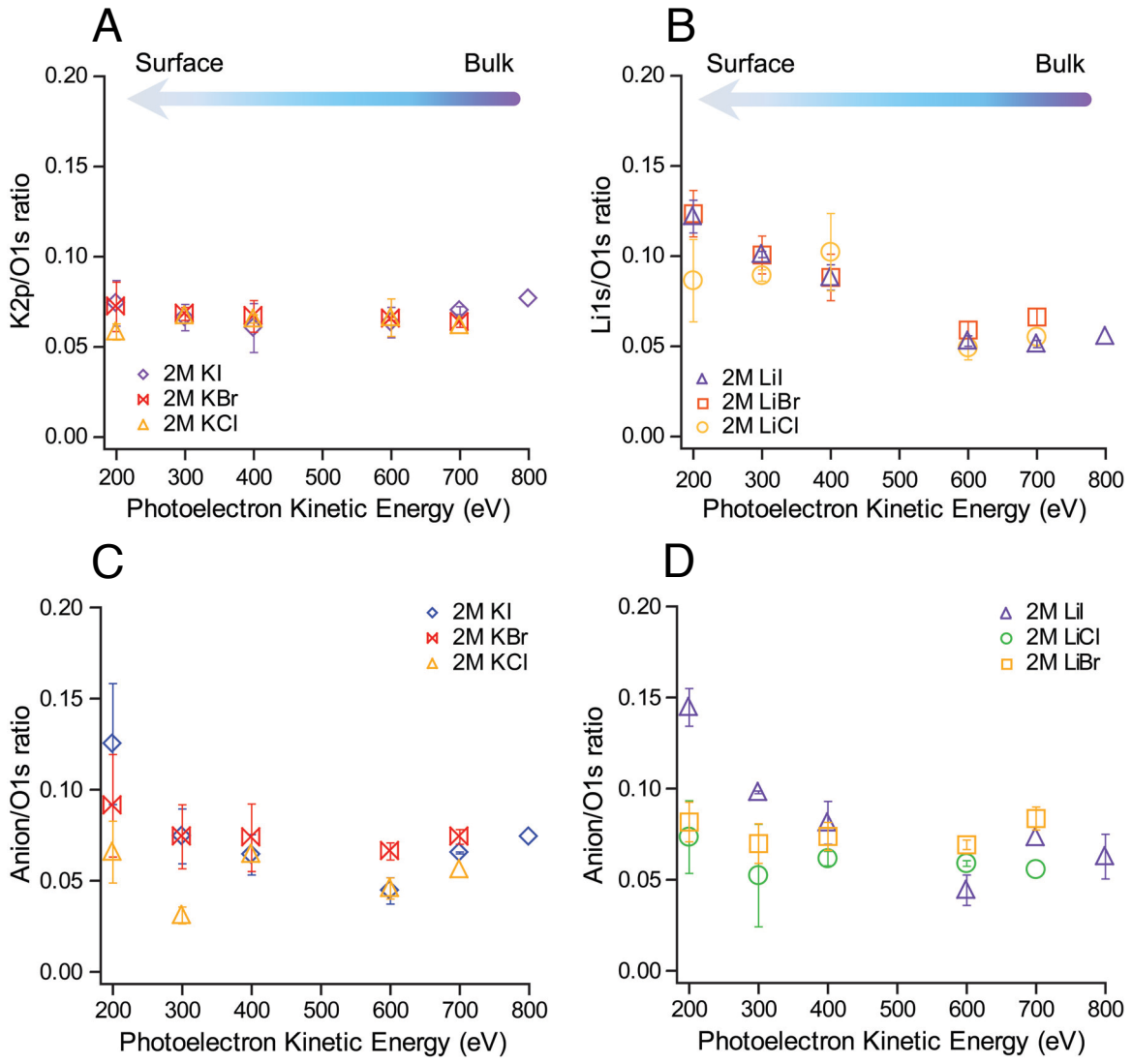

Fig. S2. Ratios of normalized cation and water oxygen XPS signals plotted vs. photoelectron KE (probe depth) for (*A*) 2 M potassium halide and (*B*) 2 M lithium halide solutions. Ratios of normalized anion and water oxygen XPS signals plotted vs. photoelectron KE (probe depth) for (*C*) 2 M potassium halide and (*D*) 2 M lithium halide solutions.

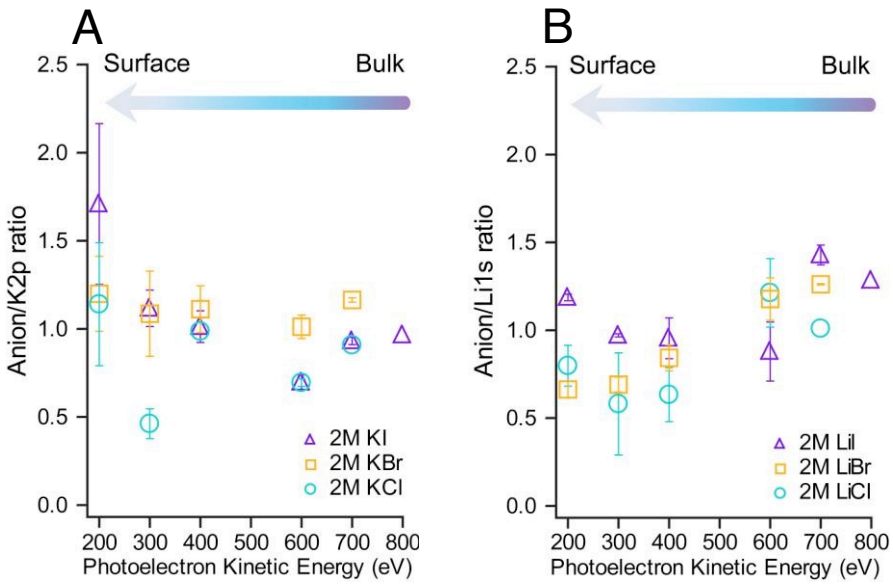

Fig. S3. Ratios of normalized anion and cation XPS signals plotted vs. photoelectron KE (probe depth) for (*A*) 2 M potassium halide and (*B*) 2 M lithium halide solutions.

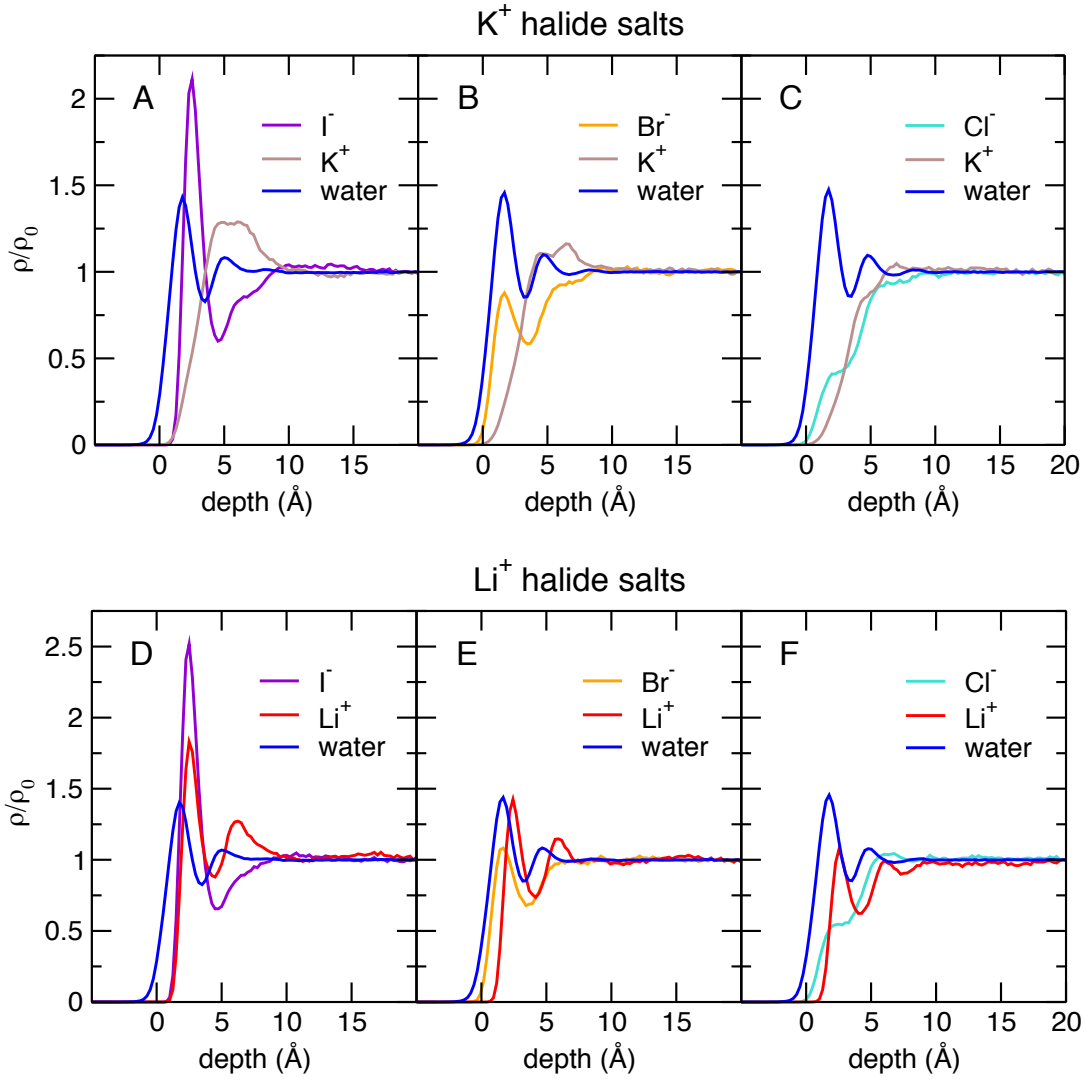

Fig. S4. Density profiles of ions and water oxygen atoms from MD simulations of (*A*) 2 M, (*B*) 2 M KBr, (*C*) 2 M KCl, (*D*) 2 M LiI, (*E*) 2 M LiBr, and (*F*) 2 M LiCl solutions. The density profile of each species has been calculated with respect to the instantaneous solution-air interface and divided by the corresponding bulk density, ρ_0. The interface is located at depth = 0.

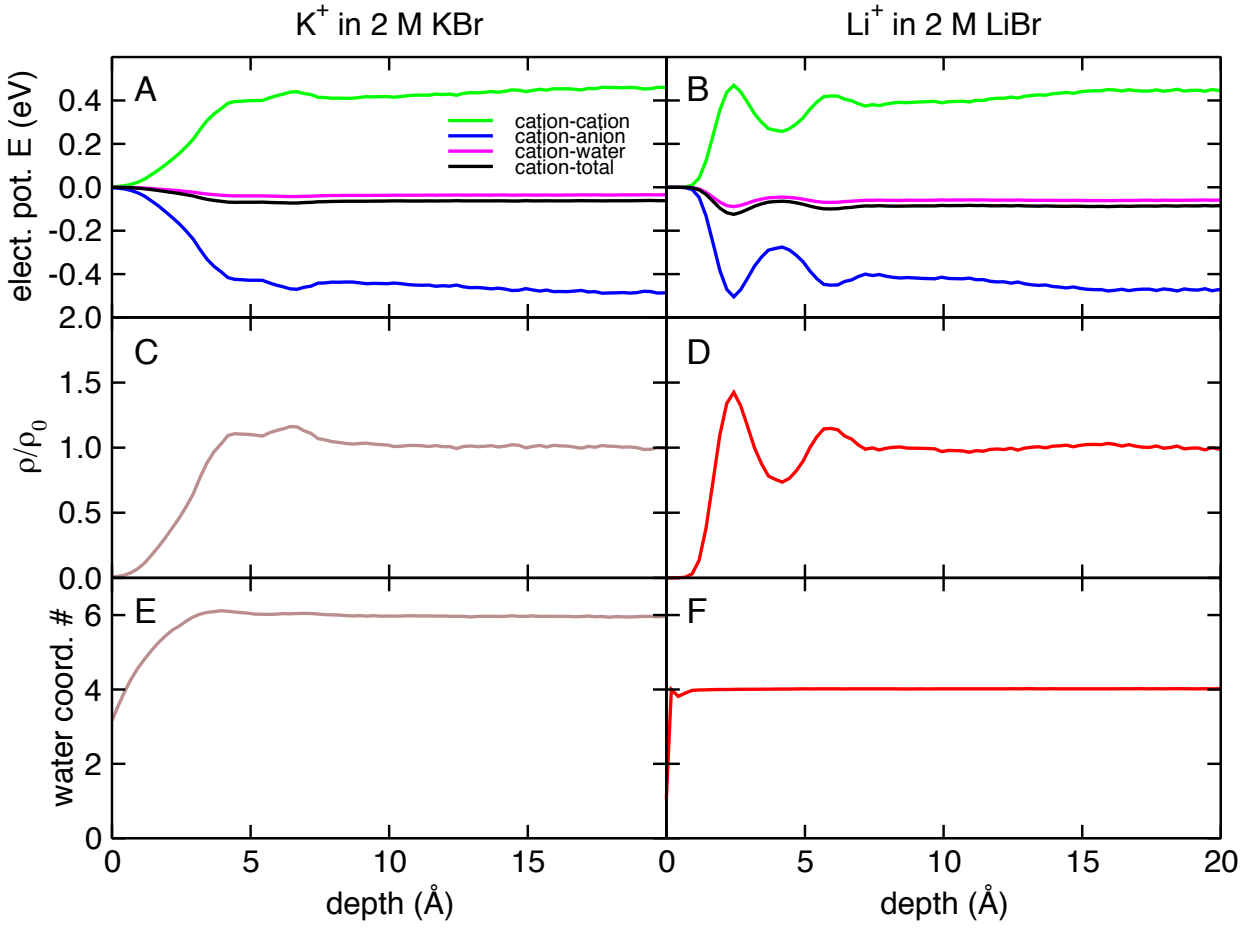

Fig. S5. Depth-dependence of the electrostatic interaction energies of (*A*) K^+ ions in 2 M KBr and (*B*) Li^+ ions in 2 M LiBr. The green curves are contributions from cation-cation interactions, the blue curves from cation-anion interactions, and the magenta curves from cation-water interactions. The black curves are the total electrostatic interaction energies. (*C*) Density profile for K^+ ions in 2 M KBr. (*D*) Density profile for Li^+ in 2 M LiBr. (*E*) Number of water molecules in the first solvation shell of K^+ in 2 M KBr. (*F*) Number of water molecules in the first solvation shell of Li^+ in 2 M LiBr. All quantities in this figure were calculated with respect to the instantaneous solution-air interface. The interface is located at depth = 0.

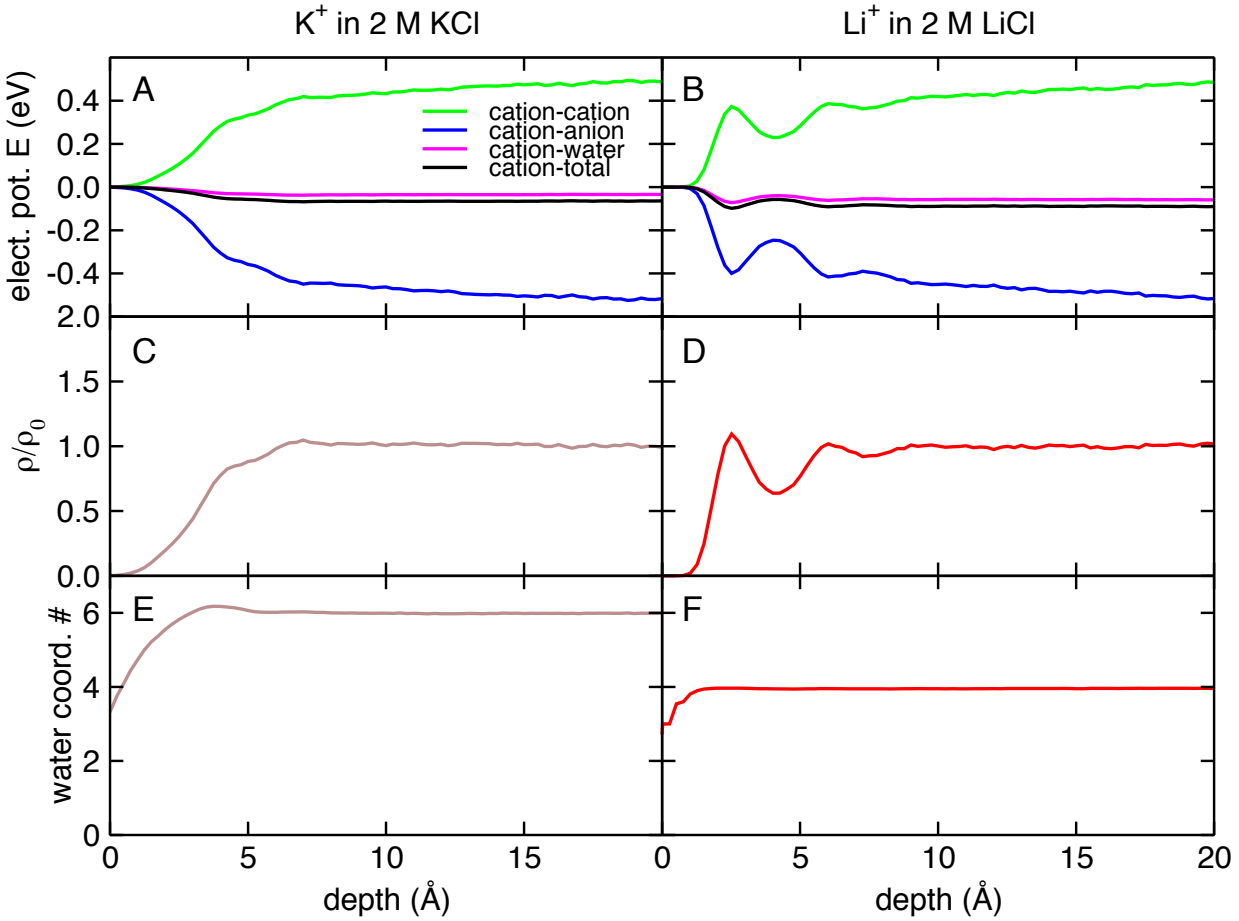

Fig. S6. Depth-dependence of the electrostatic interaction energies of (*A*) K^+ ions in 2 M KCl and (*B*) Li^+ ions in 2 M LiCl. The green curves are contributions from cation-cation interactions, the blue curves from cation-anion interactions, and the magenta curves from cation-water interactions. The black curves are the total electrostatic interaction energies. (*C*) Density profile for K^+ ions in 2 M KCl. (*D*) Density profile for Li^+ in 2 M LiCl. (*E*) Number of water molecules in the first solvation shell of K^+ in 2 M KCl. (*F*) Number of water molecules in the first solvation shell of Li^+ in 2 M LiCl. All quantities in this figure were calculated with respect to the instantaneous solution-air interface. The interface is located at depth = 0.

Table S1. Force field parameters and instantaneous interface convolution parameters. The force field parameters for water O and H atoms are from the SPC/E water model (5). The ion force field parameters are from Horinek et al. (set 2 for Li^+, K^+, and I^-; set 1 for Cl^- and Br^-) (6).

Atom	q (e)	σ (Å)	ε (kJ/mol)	ξ (Å)	η
O	–0.8476	3.166	0.65	2.4	1.0
H	+0.4238	–	–	–	–
Li^+	+1.0	1.474	0.65	0.0	0.0
K^+	+1.0	2.945	0.65	0.0	0.0
Cl^-	–1.0	4.394	0.416	0.0	0.0
Br^-	–1.0	4.834	0.2106	2.55	0.477
I^-	–1.0	5.014	0.985	2.7	3.35

References

1. Willard AP & Chandler D (2010) Instantaneous liquid interfaces. *J. Phys. Chem. B* 114:1954-1958.
2. Stern AC, Baer MD, Mundy CJ, & Tobias DJ (2013) Thermodynamics of iodide adsorption at the instantaneous air-water interface. *J. Chem. Phys.* 138:114709.
3. Ottosson N, Faubel M, Bradforth SE, Jungwirth P, & Winter B (2010) Photoelectron spectroscopy of liquid water and aqueous solution: Electron effective attenuation lengths and emission-angle anisotropy. *J. Electron Spectrosc. Relat. Phenom.* 177:60-70.
4. Thurmer S*, et al.* (2013) Photoelectron angular distributions from liquid water: effects of electron scattering. *Phys. Rev. Lett.* 111:173005.
5. Berendsen HJC, Grigera JR, & Straatsma TP (1987) The missing term in effective pair potentials. *Journal of Physical Chemistry* 91(24):6269-6271.
6. Horinek D*, et al.* (2009) Specific ion adsorption at the air/water interface: The role of hydrophobic solvation. *Chem. Phys. Lett.* 479:173-183.